The Astrophysical Journal, 784:77 (9pp), 2014 March 20 doi:10.1088/0004-637X/784/1/77

REVEALING THE LOCATION AND STRUCTURE OF THE ACCRETION DISK WIND IN PDS 456

J. Gofford[1], J. N. Reeves[1,2], V. Braito[3], E. Nardini[1], M. T. Costa[1], G. A. Matzeu[1], P. O'Brien[4], M. Ward[5], T. J. Turner[2], and L. Miller[6]
[1] Astrophysics Group, School of Physical and Geographical Sciences, Keele University, Keele, Staffordshire, ST5 5BG, UK; j.a.gofford@keele.ac.uk
[2] Center for Space Science and Technology, University of Maryland Baltimore County, 1000 Hilltop Circle, Baltimore, MD 21250, USA
[3] INAF-Osservatorio Astronomico di Brera, Via Bianchi 46 I-23807 Merate (LC), Italy
[4] Department of Physics and Astronomy, University of Leicester, University Road, Leicester, LE1 7RH, UK
[5] Department of Physics, University of Durham, South Road, Durham, DH1 3LE, UK
[6] Department of Physics, University of Oxford, Denys Wilkinson Building, Keble Road, Oxford, OX1 3RH, UK
Received 2013 December 18; accepted 2014 February 13; published 2014 March 5

ABSTRACT

We present evidence for the rapid variability of the high-velocity iron K-shell absorption in the nearby ($z = 0.184$) quasar PDS 456. From a recent long *Suzaku* observation in 2013 ($\sim$1 Ms effective duration), we find that the equivalent width of iron K absorption increases by a factor of $\sim$5 during the observation, increasing from $<$105 eV within the first 100 ks of the observation, toward a maximum depth of $\sim$500 eV near the end. The implied outflow velocity of $\sim$0.25 c is consistent with that claimed from earlier (2007, 2011) *Suzaku* observations. The absorption varies on timescales as short as $\sim$1 week. We show that this variability can be equally well attributed to either (1) an increase in column density, plausibly associated with a clumpy time-variable outflow, or (2) the decreasing ionization of a smooth homogeneous outflow which is in photo-ionization equilibrium with the local photon field. The variability allows a direct measure of absorber location, which is constrained to within $r = 200$–$3500\ r_g$ of the black hole. Even in the most conservative case, the kinetic power of the outflow is $\gtrsim$6% of the Eddington luminosity, with a mass outflow rate in excess of $\sim$40% of the Eddington accretion rate. The wind momentum rate is directly equivalent to the Eddington momentum rate which suggests that the flow may have been accelerated by continuum scattering during an episode of Eddington-limited accretion.

Key words: black hole physics – quasars: individual (PDS456) – X-rays: galaxies

Online-only material: color figures

1. INTRODUCTION

Outflows (or winds) are likely to be a natural and unavoidable result of the accretion process (e.g., King 2003; Ohsuga et al. 2009). In active galactic nuclei (AGNs), the feedback associated with outflowing matter is believed to play an important role in shaping the co-evolution of the central massive black hole and the host galaxy (King 2003; Di Matteo et al. 2005), plausibly leading to the observed AGN–host-galaxy relationships, e.g., $M - \sigma$ (King 2010; Zubovas & King 2012; McQuillin & McLaughlin 2013). Recently, a number of massive ($N_H \sim 10^{23}$ cm^{-2}), high-velocity ($v_{out} \gtrsim 0.1$ c) outflows, as revealed through the presence of blue-shifted Fe K absorption at $E > 7$ keV in the rest-frame, have been found in luminous AGNs (e.g., Pounds et al. 2003; Chartas et al. 2003; Reeves et al. 2009; Tombesi et al. 2010; Gofford et al. 2013). The large wind velocity—which indicates an origin directly associated with the accretion disk, hence leading them to be dubbed "disk winds"—implies that the wind may be energetically significant in terms of feedback (i.e., $L/L_{bol} \sim 0.5\%$–5%; Hopkins et al. 2010; Di Matteo et al. 2005).

Nonetheless, one key determination currently lacking is a direct measurement of the wind location with respect to the central black hole, which is of fundamental importance when it comes to determining the wind energetics. Previous studies of the disk-wind phenomenon have employed simple geometric and kinematic relations to constrain the location of the absorbing gas (e.g., see Tombesi et al. 2012, 2013 for an outline of these arguments), but these arguments can lead to considerable uncertainties on the gas location which makes it difficult to confidently determine the wind energetics. The best way to overcome these limitations it to directly determine the location of the absorbing gas by establishing how it varies over short timescales. However, while such line variability has sometimes been observed in soft X-ray grating spectra below $E = 2$–3 keV, hence leading to robust constraints on the location of the soft X-ray warm absorber in a number of AGNs, e.g., in MRK 509 (Kaastra et al. 2012) and MR 2251-178 (Reeves et al. 2013), to date it has proven much more difficult to measure the necessary line variability at harder X-ray energies (i.e., $E > 7$ keV) where modern detectors tend to be less sensitive (e.g., Giustini et al. 2011). In this work, we overcome these limitations and report the first direct constraints on the location of a high-velocity Fe K disk wind, as measured in the powerful quasar PDS 456.

PDS 456 ($z = 0.184$) is a luminous ($L_{bol} = 10^{47}$ erg s^{-1}; Simpson et al. 1999; Reeves & Turner 2000) radio-quiet quasar which harbors one of the most powerful Fe K disk winds currently known (Reeves et al. 2009, hereafter "R09"). *XMM-Newton* first found the X-ray spectrum to be absorbed at $E > 7$ keV in 2001, with the absorption attributable to highly ionized iron (Reeves et al. 2003). A subsequent *Suzaku* observation in 2007 revealed two highly significant absorption lines at 9.08 and 9.66 keV in the quasar rest-frame (R09). These lines are most likely associated with resonant absorption from Fe XXV Heα and Fe XXVI Lyα, which hence implies an outflow velocity in the range $v_{out} \sim 0.25$–0.3 c (R09). In a more recent *Suzaku* observation (2011), we again found a broad absorption trough at $\sim$9 keV in the source rest-frame (Reeves et al. 2014,

Table 1
Summary of PDS 456 Observations with *Suzaku*

Parameter	2007	2011	2013a	2013b	2013c
Sequence number	701056010	705041010	707035010	707035020	707035030
Start date, time (UT)	2007 Feb 24, 17:58	2011 Mar 16, 15:00	2013 Feb 21, 21:22	2013 Mar 03, 19:43	2013 Mar 08, 12:00
End date, time (UT)	2007 Mar 01, 00:51	2011 Mar 19, 08:33	2013 Feb 26, 23:51	2013 Mar 08, 12:00	2013 Mar 11, 09:00
Duration (ks)[a]	...	...	0–440.914	858.026–1262.252	1262.253–1510.654
Exposure (ks)	190.6	125.6	182.3	164.8	108.3
Count rate (10^{-2} counts s^{-1})	27.22 ± 0.09	14.1 ± 0.08	6.74 ± 0.04	4.35 ± 0.04	5.15 ± 0.05
F(0.5–2 keV)[b]	3.46	1.36	0.59	0.29	0.45
F(2–10 keV)[b]	3.55	2.84	2.07	1.52	1.51

Notes.
[a] Time-splits for the 2013 sequences.
[b] Continuum flux, in units of $\times 10^{-12}$ erg cm^{-2} s^{-1}.

hereafter "R14"), and we found that the absorption in both 2007 and 2011 could be due to the same flow of gas which is in photo-ionization equilibrium with the emergent X-ray emission. However, due to the large time difference between the observations, direct constraints could not be placed on the radial location of the absorbing gas. Even so, we were able to describe the absorption in both observations using the self-consistent disk-wind models of Sim et al. (2008, 2010a), hence showing the variable wind profile to be consistent with a radiatively driven flow launched from the inner accretion disk (R14).

In this paper, we report the first results from our extensive observational campaign of PDS 456 with the *Suzaku*, *XMM-Newton* and *NuSTAR* satellites in 2013 (February–September). Here, we focus specifically on characterizing the remarkable spectral variability exhibited by the Fe K wind during the new long *Suzaku* observation (2013 February–March), and use this variability to place the first direct constraints on the wind location. A full spectral analysis of both these *Suzaku* data and the accompanying contemporaneous *XMM-Newton* and *NuSTAR* campaign will be presented in forthcoming work.

2. DATA REDUCTION

Suzaku (Mitsuda et al. 2007) observed PDS 456 at the aim-point of the X-ray Imaging Spectrometers (XIS; Koyama et al. 2007). Due to scheduling constraints, the observation comprised three sequences: the first (ObsID: 707035010, hereafter 2013a) has a duration of ~441 ks and was obtained between 2013 February 21–26, while the second (ObsID: 707035020, hereafter 2013b) and third (ObsID: 707035030; hereafter 2013c) were obtained consecutively between 2013 March 3–11 and have durations of ~404 ks and ~245 ks, respectively. The effective duration of the campaign was ~1 Ms. A detailed summary of the three sequences is given in Table 1. Analogous parameters for the 2007 and 2011 *Suzaku* observations are also noted for comparison.

Following the process outlined in the *Suzaku* data reduction guide[7], we extract spectral data for the functioning XIS(0, 1, 3) CCDs in each sequence using HEASOFT (v6.14) and the latest version of the calibration database (2013 August). Data were selected from the 3×3 and 5×5 edit-modes and then processed according to the recommended screening criteria. XIS source products were selected from circular regions 1.′5 in radius, with the background contribution estimated from four offset circular regions of equal radius. Spectra and light curves were extracted from the cleaned event files using XSELECT, with the response matrices (RMF) and ancillary response files (ARF) for each detector created using the XISRMFGEN and XISSIMARFGEN tasks. After verifying their consistency, we created an XIS-FI spectrum for each sequence by combining the spectra and response files for each set of front-illuminated (FI) XIS 0 and XIS 3 CCDs; the net on-source exposures were 182.3 ks, 164.8 ks and 108.3 ks for sequences 2013a, 2013b, and 2013c, respectively, culminating in a net *Suzaku* exposure of 455.4 ks for PDS 456 during the 2013 observation.

Unfortunately, PDS 456 is not detected by the hard X-ray detector (Takahashi et al. 2007). However, a definitive hard X-ray spectrum has since been obtained by *NuSTAR* in September 2013. Details of these observations are deferred to future work.

3. SPECTRAL ANALYSIS

In this work, we focus our attention on the data obtained by the FI XIS CCDs because they provide the highest effective area and lowest background rate in the crucial Fe K band. For analysis, we grouped each of the XIS-FI spectra to the approximate half-width at half-maximum energy resolution of the XIS (i.e., ~60 eV at 6 keV), and adopted an additional minimum grouping of 40 counts per energy bin such that the χ^2 minimization technique could be used during spectral fitting. We consider the XIS-FI data between 0.6–10 keV when fitting the data, ignoring between $1.7 - 1.9$ keV due to uncertainties with the XIS Si detector edge. Unless otherwise stated, all statistics are given relative to the Fe K band (i.e., between 5–10 keV) to ensure that they are driven by the Fe K absorption rather than the soft X-ray data which typically dominates the statistics in XIS data. Parameter errors are quoted at the 90% confidence interval (corresponding to $\Delta\chi^2 = 2.71$ for 1 parameter of interest), while the standard 1σ error bars are displayed in all plotted spectra. We adopt values of $H_0 = 70$ km s^{-1} Mpc^{-1}, and $\Omega_{\Lambda_0} = 0.73$ throughout.

3.1. Individual Sequences

We began our analysis by considering the XIS-FI spectra from each sequence individually. Figure 1 shows a raw comparison between all of the *Suzaku* observations of PDS 456 taken to date (2007, 2011, 2013a–c). The data are unfolded against a simple $\Gamma = 2$ power-law model and uncorrected for Galactic absorption. It is apparent from Figure 1 that all of the 2013 sequences are reasonably hard ($\Gamma = 1.27$ between 3–5 keV, compared to $\Gamma = 2.3$–2.4 in 2007), with a spectral shape reminiscent of (but still harder than) that seen in the absorbed 2011 observation (R14). The soft X-ray flux is much lower in

[7] http://heasarc.gsfc.nasa.gov/docs/suzaku/analysis/abc/

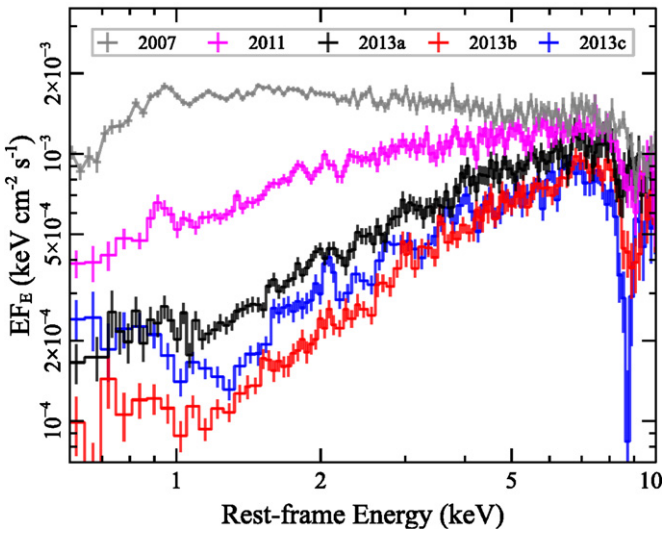

Figure 1. Comparison of spectra from all *Suzaku* observations of PDS 456 to date (2007, 2011, 2013a–c). The 2007 observation (gray spectrum) is the brightest, with a roughly power-law spectral shape, while the 2011 and 2013 observations get progressively harder and more absorbed. Absorption is persistent at ∼9 keV in all of the *Suzaku* observations, and is especially prominent during the 2013 observation.

(A color version of this figure is available in the online journal.)

Table 2
Baseline Continuum Parameters

Component	Parameter	2013a	2013b	2013c
tbabs	$N_{H,Gal}$		2×10^{21} cm^{-2}	
powerlaw	Γ	2.4*	...	...
	Norm[a]	2.14 ± 0.06	1.69 ± 0.05	1.45 ± 0.05
pcfabs$_1$	log N_H[b]	21.9 ± 0.1	21.9[t]	21.9[t]
	f_{cov} (%)	77 ± 3	86 ± 4	>95
pcfabs$_2$	log N_H[b]	22.9 ± 0.1	22.9[t]	22.9[t]
	f_{cov} (%)	63 ± 3	73 ± 2	50 ± 4
bbody	kT (eV)	106 ± 5	106[t]	106[t]
	Norm[c]	1.7 ± 0.3	0.9 ± 0.2	2.4 ± 0.5
zgauss	E (keV)	6.94 ± 0.10	6.94[t]	6.94[t]
	σ (eV)	400*	...	...
	EW (eV)	220 ± 30	290 ± 40	330 ± 40

Notes.
[a] Power-law normalization, in units of 10^{-3} photon keV^{-1} cm^{-2} s^{-1}.
[b] Logarithm of the absorber column density. Unit of N_H is cm^{-2}.
[c] Black-body normalization in units of $10^{-5}(L_{39}/D_{10}^2)$, where L_{39} is the source luminosity in units of 10^{39} erg s^{-1} and D_{10} is the distance to the source in units of 10 kpc.
* Indicates a parameter fixed during fitting.
[t] Parameter tied during fitting.

2013 than in the relatively unabsorbed 2007 observation (R09, R14), with a mean $\langle F_{0.5-2} \rangle = 4.43 \times 10^{-13}$ erg cm^{-2} s^{-1} in 2013 compared to 3.46×10^{-12} erg cm^{-2} s^{-1} in 2007, while $\langle F_{2-10} \rangle$ is also lower (see Table 1). These factors suggest that PDS 456 is again heavily absorbed during the 2013 *Suzaku* epoch. This is further alluded to by the deep Fe K absorption trough at ∼9 keV (rest-frame) in sequences 2013b and 2013c (see Figure 2). The remainder of this work focusses on characterising this absorption in greater detail.

In order to probe the absorption system, it was first necessary to parameterize the continuum. We find that a partially covered absorption model provides a good simultaneous fit to the three 2013 sequences. In summary, and noting that a fully detailed spectral de-composition of these data is to be presented in subsequent work, we parameterize the continuum with a phenomenological model of the form tbabs(pcfabs$_1$ × pcfabs$_2$ × powerlaw+bbody+zgauss), where tbabs (Wilms et al. 2000) accounts for the Galactic absorption column density of $N_{H,Gal} = 2 \times 10^{21}$ cm^{-2} (Dickey & Lockman 1990), powerlaw is the underlying power-law continuum, pcfabs$_{1,2}$ are two neutral partially covering absorbers, and bbody is an ad-hoc black-body with $kT \sim (106 \pm 5)$ eV that provides some necessary soft emission at $E \lesssim 1.5$ keV. This soft component may be associated with the reprocessed emission from the outer wind, e.g., similar to what is seen in some wind-dominated ultra-luminous X-ray sources (Middleton et al. 2014), with the intrinsic emission of the accretion disk, or have another origin. For simplicity, we opt to not absorb the bbody component with the partially covering gas to prevent degeneracies between its normalization and the gas covering fraction. We note, however, that an equivalent description of the data can be achieved if the bbody is absorbed; the ensued parameters for the Fe K absorption are also unaffected by how the soft component is modeled. A full discussion regarding the origin of the soft component is deferred to future work.

The zgauss component in our baseline model corresponds to the broad ionized emission line at ∼6.9 keV (rest-frame), which might be associated with light scattered from the disk wind (see R14 for a discussion); we fit this broad profile with a (fixed) width of $\sigma = 400$ eV, as found for the 2011 observation by R14. We adopt assume a (fixed) power-law slope of $\Gamma = 2.4$ to ensure consistency with both the bright (unabsorbed) 2007 *Suzaku* observation (R09) and the new *NuSTAR* hard X-ray spectrum (which will be presented in subsequent work). Allowing Γ to be free to vary from this value does not result in a statistical improvement to the fit. We account for the changes in intra-sequence curvature by allowing the covering fraction (f_{cov}) of the partially covering absorbers to vary freely; covering fractions of $f_{cov,1} \simeq 0.75$–0.95 and $f_{cov,2} \simeq 0.45$–0.75, for tied column densities of $\log N_{H,1} = 21.9 \pm 0.1$ and $\log N_{H,2} = 22.9 \pm 0.1$, respectively, are sufficient to model all three sequences. Note that while we do not discuss the physical nature of the partially covering gas in detail here, it could plausibly be associated with either clumps within a disk wind (e.g., R14) or possibly with clouds in the more extended broad line region (BLR; e.g., as has been suggested in NGC 1365, Risaliti et al. 2009; Mrk 766, Risaliti et al. 2011 and MR 2251-178; Reeves et al. 2013). Full parameters for the baseline model are noted in Table 2.

In general, this simple phenomenological model is consistent with that employed by R14 to jointly describe the 2007 and 2011 observations, and we find that it again provides a good account of the spectral shape in 2013. The full fit statistic between 0.6–10 keV is $\chi^2/\nu = 716.2/505$, with the strong absorption in the Fe K band being the main deviation from the continuum model (see Figure 2, panels (d)–(f)). Figure 2(a)–(c) shows the fluxed 2013 sequences and their best-fit model. Note that obtaining an accurate description of the spectral variability during 2013 appears to be contingent on the source being obscured by two layers of partially covering gas. This is consistent with what was found by R14 from the analysis of the previous 2007 and 2011 *Suzaku* spectra.

It is clear that despite the baseline model providing a reasonable fit to the continuum the fit statistic between 5–10 keV (rest-frame) is still poor due to the strong absorption ($\chi^2/\nu = 383.2/190$ over this energy range, $P_{null} = 4.1 \times 10^{-15}$). The ratio spectra (see Figure 2(d)–(f)) demonstrate that the depth of

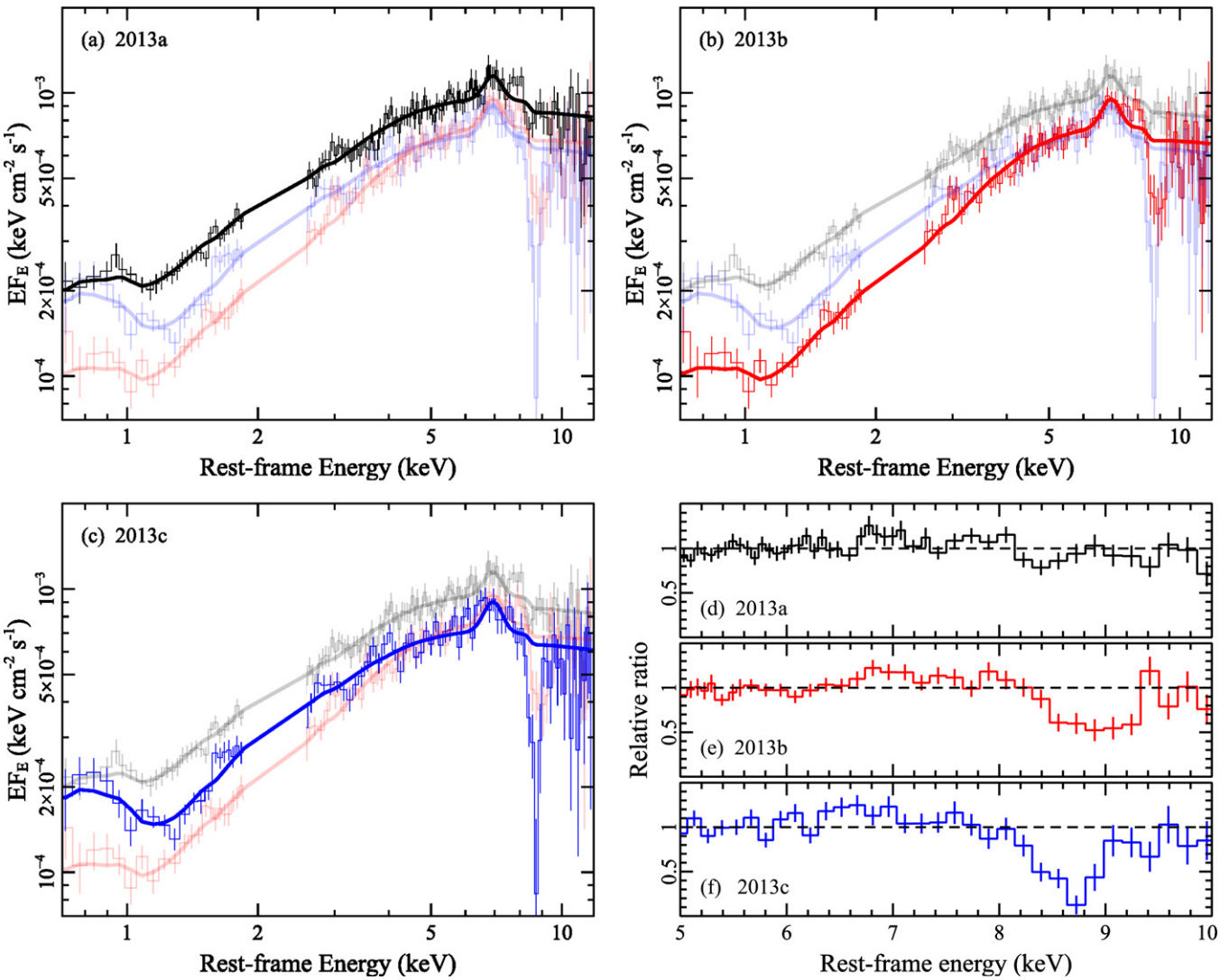

Figure 2. Fluxed rest-frame spectra from the three 2013 *Suzaku* sequences. Panels (a)–(c) shows the unfolded spectra for each of the 2013 sequences and their corresponding best-fit continuum model. Sequences 2013a, 2013b, and 2013c are shown by the black, red, and blue spectra, respectively. Note that these fluxed spectra have been created by unfolding the data and model against a $\Gamma = 2$ power-law, with the best-fitting continuum model overlaid afterward; they have not been unfolded against the best-fit model including an absorption line. Panels (d)–(f) show the ratio spectra of the three 2013 sequences against the baseline partially covered continuum model described in the text. Note the strong increase in depth of the Fe K absorption from sequence 2013a to 2013c. Data have been re-binned to the approximate FWHM resolution of the XIS-FI for clarity.

(A color version of this figure is available in the online journal.)

absorption increases across the three sequences, being weakest in the 2013a sequence and strongest in 2013c. Modeling the profile with a Gaussian (see Table 3 for parameters) indicates that, for a best-fit variable width of $\sigma = (250 \pm 60)$ eV which was left tied between the sequences, the equivalent width (EW) of absorption increases by a factor of $\sim$5 throughout the observation, from $<$110 in 2013a to (490 ± 70) eV in 2013c. The line centroid also appears to be at a lower energy in 2013c than in 2013b at the 90% level, decreasing from (8.80 ± 0.10) to (8.65 ± 0.06) keV, indicative of a possible change in outflow velocity or ionization state. The Gaussian parameterization results in a $\Delta\chi^2/\nu = -159.2/6$ improvement with respect to the baseline continuum, for an overall fit statistic of $\chi^2/\nu = 224.0/184$ in the Fe K band.

Having parameterized the profile, we replaced the Gaussian with a custom generated XSTAR (v2.21bn13, Bautista & Kallman 2001) absorption table with a $\Gamma = 2.4$ illuminating continuum and a turbulent line broadening of $v_{\rm turb} = 5000$ km s^{-1}. This value for $v_{\rm turb}$ was adopted as it provided the best description of the broadness of the absorption profile. We also tried other grids but found that in grids with $v_{\rm turb} = (1000, 3000)$ km s^{-1} the saturated too quickly to fit the observed breadth and EW of the profile, while $v_{\rm turb} = 10{,}000$ km s^{-1} was simply too broad to provide a satisfactory fit to the data. Using the $v_{\rm turb} = 5000$ km s^{-1} absorption table, we thus investigated two scenarios that could give rise to the observed line variability. In the first (Model A), we tied the column density ($N_{\rm H}$) between the sequences but allowed the ionization parameter (ξ) to vary. This scenario corresponds to an absorber that remains persistently in the line of sight (LOS) but whose ionization changes (decreases) during the observation. In the second scenario (Model B), we allowed the $N_{\rm H}$ to vary but tied the ξ. This scenario is intended to model the case where an inhomogeneous absorber crosses the LOS during the observation, with $N_{\rm H}$ subsequently increasing. The outflow velocity $v_{\rm out}$ was initially allowed to vary in both cases.

The parameters for both of these models are listed in Table 3. In both cases, the outflow velocity of the absorber appearing to

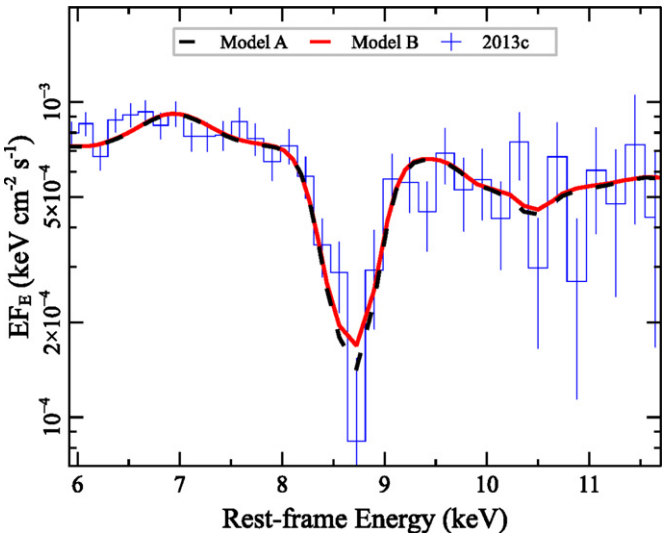

Figure 3. Fluxed rest-frame spectrum from sequence 2013c overlaid with the best-fit XSTAR models for the deep absorption line. The fit for Models A and B, which, as described in the text, provide statistically equivalent descriptions of the observed profile, are shown by the black (dashed) and red (solid) lines, respectively. As before, the fluxed spectra has been unfolded against a reference $\Gamma = 2$ power-law continuum with the model overlaid afterward; they have not been unfolded against the best-fitting model.

(A color version of this figure is available in the online journal.)

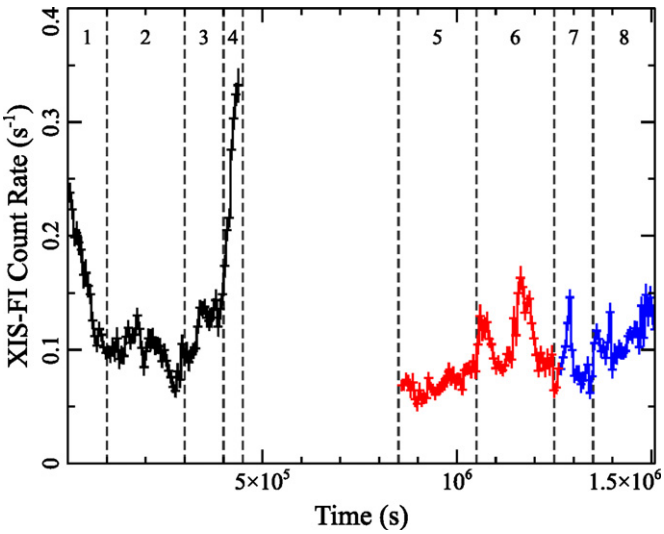

Figure 4. Combined XIS 03 0.5–10 keV light curves for the 2013 *Suzaku* data, binned to orbital (5760 s) bins. Light curves for sequences 2013a, 2013b, and 2013c are shown by the black, red, and blue data points, respectively. The gap in the coverage corresponds to the one week scheduling gap between 2013a and 2013b. The vertical dotted lines mark boundaries of the spectral slices 1–8 as described in the text. Note the strong flare between 400–450 ks (slice 4) at the end of 2013a.

(A color version of this figure is available in the online journal.)

Table 3
Iron K Absorption Parameters for 2013 Sequences

	Parameter	2013a	2013b	2013c
	Gaussian			
(1)	Line energy (keV)	8.88[t]	8.88 ± 0.10	8.65 ± 0.06
(2)	σ-width (eV)	250[t]	250 ± 60	250[t]
(3)	EW (eV)	<110	310 ± 80	490 ± 70
(4)	$\Delta\chi^2/\nu$	...	−42.1/3	−129.6/3
	XSTAR			
(5)	$\log(\xi/\mathrm{erg\,cm\,s^{-1}})$	>4.35	3.8 ± 0.1	3.4 ± 0.1
(6)	$\log(N_{\rm H}/\mathrm{cm^{-2}})$	<22.9	23.4 ± 0.2	23.9 ± 0.1
(7)	$v_{\rm out}/c$	...	-0.244 ± 0.008	-0.227 ± 0.007

Notes. (1) Rest-frame energy of Gaussian absorption line; (2) σ-width of Gaussian; (3) equivalent width of Gaussian; (4) change in χ^2/ν upon adding a Gaussian line to the baseline continuum model. A negative value indicates a statistical improvement; (5) XSTAR parameters for Model A, in which $\log(\xi/\mathrm{erg\,cm\,s^{-1}})$ is allowed to vary for a constant $\log(N_{\rm H}/\mathrm{cm^{-2}}) = 23.6^{+0.1}_{-0.2}$; (6) XSTAR parameters for Model B, where $N_{\rm H}$ is allowed to vary at a constant $\log(\xi/\mathrm{erg\,cm\,s^{-1}}) = 3.48 \pm 0.14$; (7) inferred outflow velocity in the quasar rest-frame ($z = 0.184$). Negative values denote a net blue-shift.
[t] Indicates that a parameter was tied during fitting.

be slightly lower in 2013c than in 2013b at the $P_{\rm f\text{-}test} > 99\%$ level, which mirrors the subtle change in centroid energy found during Gaussian fitting (see Table 3). Statistically, the two models yield equivalently good fits to the Fe K band, with $\chi^2/\nu = 211.2/184$ and $\chi^2/\nu = 208.9/184$ for Model A and Model B, respectively. A comparison of the two fits, as applied to sequence 2013c, is shown in Figure 3. It is evident that both models give a good description of the data from the time-averaged sequences.

3.2. Time-sliced Spectra

The composite light curve (see Figure 4) indicates that the X-ray flux for PDS 456 is variable during the 2013 *Suzaku* observation. This is most apparent in Sequence 2013a, which has a strong $\times 3$–4 flare in flux between 400–450 ks. Smaller flares ($\times 1.5$–2) are also evident in the latter half of sequence 2013b, but in general the later two sequences appear to be in a state of relatively constant flux. Unfortunately, the scheduling gap between sequences 2013a and 2013b occurs during the large flare, meaning that we are unable to fully trace how it evolves with time. Even so, the remaining data are all of sufficient quality to enable a time-resolved analysis of the absorption profile, thereby sampling its variability over shorter timescales. Guided by the visual properties of the light curve we thus split the spectrum into a total of eight slices; these are overlaid on the light curve in Figure 4. Slices 1 and 2 trace the decline and subsequent quiescent period in the first half of sequence 2013a, while slices 3 and 4 trace both the initial onset of the flare and the flare itself, respectively. Slices 5–8 then split sequences 2013b and 2013c roughly in half, avoiding any smaller flares. The timing periods for each slice are noted in Table 4.

We thus re-sampled the properties of the absorption using the time-sliced spectra, first with a simple Gaussian and then with XSTAR. The baseline model (as described earlier) again provides a good description of all eight slices; the rest-frame 6–10 keV ratio spectra with respect to this model are shown in Figure 5. In general, the time-sliced results are consistent with those for the time-averaged sequences: Fe K absorption is not statistically required at the start of the observation (slices 1–3), with the first tentative detection (i.e., at $\geqslant 90\%$ confidence) occurring in slice 4. The absorption then gets sequentially stronger through slices 5 and 6, before reaching an eventual maximum depth (and highest significance of $\Delta\chi^2/\nu = -54.5/3$) in slice 7. In slice 8, the line seems to get slightly less significant, but its overall parameters are consistent with those found in slice 7. For a common line width of $\sigma = (240 \pm 70)$ eV, the EW of the profile increases from <105 to (480 ± 125) eV in the ~1 Ms between slices 1 and 7, i.e., by a factor ~5. The line centroid is again found to be ~8.6–8.9 keV in the quasar rest-frame, consistent with what was found before in the time-averaged sequences.

Table 4
Iron K Absorption Parameters from the Spectral Slices

Slice	Time (ks)	Energy (keV) (1)	EW (eV) (2)	$N_{\rm H}$ (3)	$\log\xi$ (4)	$v_{\rm out}/c$ (5)	Flux (6)	$\Delta\chi^2/\nu$ (7)
1	0–100	8.50^{t}	<105	<22.6	>4.28	-0.22^{t}	3.00 (6.70)	NR
2	100–300	8.50^{t}	<132	<22.8	>3.97	-0.22^{t}	1.94 (4.86)	NR
3	300–400	8.50^{t}	<257	<23.5	>3.28	-0.22^{t}	2.20 (5.05)	NR
4	400–450	8.50 ± 0.15	220 ± 100	23.0 ± 0.4	3.95 ± 0.30	-0.22 ± 0.02	4.72 (11.81)	−8.2/3
5	850–1050	8.90 ± 0.16	300 ± 120	23.4 ± 0.2	3.66 ± 0.20	-0.26 ± 0.02	1.46 (4.15)	−13.2/3
6	1050–1250	8.92 ± 0.14	300 ± 95	23.5 ± 0.2	3.62 ± 0.14	-0.27 ± 0.01	2.14 (5.19)	−24.9/3
7	1250–1350	8.63 ± 0.13	480 ± 125	23.8 ± 0.2	$3.49^{+0.07}_{-0.03}$	-0.24 ± 0.01	1.70 (4.46)	−54.5/3
8	1350–1510	8.70 ± 0.11	360 ± 100	23.7 ± 0.1	3.31 ± 0.03	-0.25 ± 0.01	2.05 (4.88)	−30.8/3

Notes. (1) Rest-frame energy of Gaussian absorption line; (2) absorption line equivalent width, for constant width of $\sigma = (240 \pm 70)$ eV; (3) XSTAR parameters for fit with variable $\log(N_{\rm H}/{\rm cm}^{-2})$ for a constant $\log(\xi/{\rm erg\,cm\,s}^{-1}) = 3.48 \pm 0.14$; (4) XSTAR parameters for fit with variable $\log(\xi/{\rm erg\,cm\,s}^{-1})$, for a constant $\log(N_{\rm H}/{\rm cm}^{-2}) = 23.6^{+0.1}_{-0.2}$; (5) outflow velocity in the quasar rest frame ($z = 0.184$). Negative values denote a net blue-shift; (6) absorbed (unabsorbed) source flux between 0.5–10 keV, in units of 10^{-12} erg cm^{-2} s^{-1}; (7) change in χ^2/ν when modeling absorption with a Gaussian. Negative values denote an improvement.
[t] Indicates that a parameter is fixed during spectral fitting.

We then tested XSTAR Models A and B from before, initially with the absorbers $v_{\rm out}$ left free to vary (except in slices 1–4, where it was tied between the slices due to the non-detections at the start of the observation). We again find that both models provide acceptable descriptions of the data, with $\chi^2/\nu = 358.2/351$ and 346.2/351 for Models A and B, respectively. The outflow velocity is in the range $v_{\rm out} \sim 0.24$–0.27 c, which is consistent with previous analyses (R09, R14). Tying $v_{\rm out}$ between the slices worsens the fit in both cases, yielding $\chi^2/\nu = 362.2/356$ and $\chi^2/\nu = 362.1/356$ for Models A and B. Full model parameters are given in Table 4. Overall, these results suggest that the line variability can be well described through a transiting inhomogeneous cloud or by ionization changes in a homogeneous absorber.

4. PHYSICAL PROPERTIES OF THE WIND

The observed line variability can be used to constrain both the properties of the absorbing gas and its location with respect to the continuum source. Here, we use the results from our models to investigate the properties of the high-velocity outflow in PDS 456.

4.1. A Recombining Absorber

In our first scenario (Model A), we showed that the line variability could be due to an absorber whose ionization parameter decreases from $\log(\xi/{\rm erg\,cm\,s}^{-1}) > 4.28$ to ∼3.31, for a constant $\log(N_{\rm H}/{\rm cm}^{-2}) \simeq 23.6$. Between when the absorption is first detected (slice 4) and when it reaches its strongest (slice 7), the ionization state of the absorber appears to decrease in proportion to the source flux; $\log(\xi/{\rm erg\,cm\,s}^{-1})$ decreases by a factor of ∼3 (in linear space) from 3.95 to 3.49, while the absorbed (unabsorbed) 0.5–10 keV flux drops by a similar factor during the same time-frame (i.e., from $F_{0.5-10} = 4.72(11.81) \times 10^{-12}$ in slice 4 to a mean $\sim\langle 1.8(4.7)\rangle \times 10^{-12}$ erg cm^{-2} s^{-1} in slices 5–8; see Table 4). This implies that the observed variability could be due to recombination within a smooth (i.e., with constant $N_{\rm H}$) outflow which is in photo-ionization equilibrium. The gradual decrease in ξ between slices 5–8 would then be due to Fe XXVI recombining into Fe XXV in delayed response to the bright flare in flux that occurs in slice 4. This scenario could potentially also account for the subtle decrease in velocity shift between slices 5/6 and slices 7/8, with the increasing contribution from Fe XXV broadening the profile and giving a lower apparent centroid energy.

If this is the case, we can estimate the electronic density, n_e, from the recombination time, $t_{\rm rec}$. The recombination time for ionic population X_i depends upon both the rate at which the X_{i+1} ions fall into population X_i, and the rate at which ions already in the X_i population fall into the X_{i-1} population. A robust formula which takes into account these effects is given by Bottorff et al. (2000):

$$t_{\rm rec}(X_i) = \left\{\alpha(X_i, T_e) n_e \left[\frac{f(X_{i+1})}{f(X_i)} - \frac{\alpha(X_{i-1}, T_e)}{\alpha(X_i, T_e)}\right]\right\}^{-1}, \quad (1)$$

where $f(X_i)$ is the fraction of ions in the X_i population, $\alpha(X_i, T_e)$ is the recombination coefficient of the X_i ion for electron temperature T_e, and n_e is the electron number density. We apply this equation to Fe XXV. The appropriate recombination coefficient is dependent upon the temperature of the gas, which is likely to be of the order $\log(T_e/{\rm K}) \simeq 7.7$ for a mean $\log(\xi/{\rm erg\,cm\,s}^{-1}) = 3.7$ (see Kallman et al. 2004, their Figure 6). At this ionization and temperature, the ionic fraction of Fe XXVI is roughly twice that of Fe XXV, while the ratio of Fe XXIV to Fe XXV recombination coefficient is around unity (see Nahar et al. 2001). Equation (1) then reduces to the familiar $t_{\rm rec}(X_i) \simeq [\alpha(X_i, T_e) n_e]^{-1}$.

We can estimate the recombination timescale through the time between the initial onset of the absorption and it reaching maximum depth. Taking the time between the end of slice 4 (450 ks) and the start of slice 7 (1.25 Ms) hence implies $t_{\rm rec} \sim$ 800 ks. Using the Fe XXV recombination coefficient from Nahar et al. (2001) appropriate for the likely electron temperature of $\log(T_e/{\rm K}) \simeq 7.7$ (see above), and a recombination time of $t_{\rm rec} \sim 800$ ks, yields $n_e = 5.5 \times 10^5$ cm^{-3} for the absorbing gas. However, it is important to note that the profile appears to grow gradually, with an ionization state which decreases with time (see Table 4), meaning that this method will overestimate the recombination timescale since it is simply measuring the time it takes for the profile to reach its maximum depth, and not the rate at which it takes the gas to actually recombine. A more physically motivated (and more conservative) way of estimating $t_{\rm rec}$ is to instead consider the ionization state of the gas directly. A conservative estimate on the recombination timescale can be obtained through the shortest time it takes for a change in ξ to be discernible in the data. At 90% confidence, this occurs between slices 6 (1.15 Ms) and slice 8 (1.35 Ms), implying that $t_{\rm rec} \sim 200$ ks, and that hence $n_e = 2 \times 10^6$ cm^{-3}.

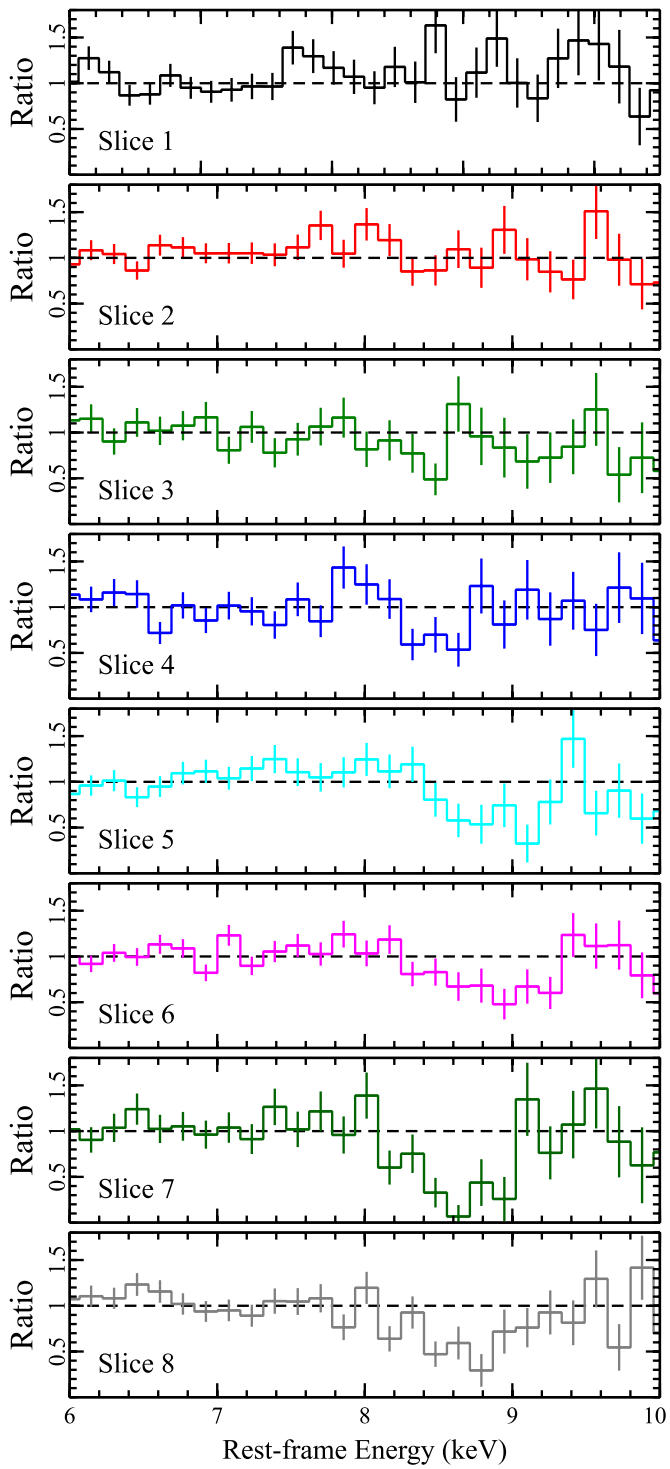

Figure 5. Ratio spectra of the *Suzaku* slices in the Fe K region, as defined in Figure 2. The iron K absorption feature becomes progressively stronger through the observation, reaching a maximum depth during slice *G* near the end of the observation. Best-fit parameters for the absorption are listed in Table 2.

(A color version of this figure is available in the online journal.)

From our estimate on n_e, we can use the definition of the ionization parameter, $\xi = L_{\rm ion}/n_{\rm H}r^2$ (Tarter et al. 1969), to estimate the distance, r, of the absorber from the ionizing continuum source. Here, $L_{\rm ion}$ is the integrated ionizing luminosity between 1–1000 Rydbergs. As it is unclear whether or not the partially covering gas is shielding the outflow, we should consider both the absorbed and unabsorbed ionizing luminosities, corresponding to the wind being shielded and unshielded by the partial coverer, respectively, to give the likely range in luminosity "seen" by the absorbing material. To first order, we can estimate $L_{\rm ion}$ by extrapolating our continuum model into the UV regime. It is worth noting, however, that estimating $L_{\rm ion}$ in this manner will probably lead an underestimate of the *true* ionizing luminosity because it neglects the excess contribution from the UV.

To roughly gauge how strongly the UV emission PDS 456 is likely to contribute to $L_{\rm ion}$, we can compare the flux predicted by our baseline X-ray model to the UV flux reported by O'Brien et al. (2005). An extrapolation of the $\Gamma = 2.4$ X-ray model predicts a (1500–2300) Å flux a factor of ∼3 lower than observed by the *Hubble Space Telescope* in the same wavelength range[8] (see O'Brien et al. 2005). The discrepancy can be accounted for with a rudimentary break in the UV-to-X-ray spectral energy distribution, hardening from $\Gamma_{\rm UV} \simeq 2.7$–$2.8$ in the UV to $\Gamma_{\rm X} = 2.4$ in the X-ray (for an $E_{\rm break} \sim 100$ eV), which increases the total inferred ionizing luminosity by a factor of ∼3. Even so, because this increase occurs predominantly in the UV regime it will essentially have no effect at Fe K where the ionization potential is significantly larger than the typical UV photon energy, i.e., ∼9 keV for Fe XXV-XXVI. Moreover, while $L_{\rm ion}$ will undoubtedly increase, the value for ξ inferred by XSTAR will also increase in proportion, so the overall ratio $L_{\rm ion}/\xi$ remains roughly constant (see Figure 9 in Giustini et al. 2011 and discussion therein). Thus, because there is no net effect of accounting for the UV break in these data, we can safely estimate $L_{\rm ion}$ based on our extrapolated X-ray model. This leads to $L_{\rm ion} = (4.0$–$22.8) \times 10^{44}$ erg s^{-1} in the shielded–unshielded cases (corrected for Galactic absorption in both cases).

Thus, for a mean $\log(\xi/{\rm erg\,cm\,s^{-1}}) = 3.7$, and remembering that electron density (n_e) is related to the gas density ($n_{\rm H}$) by the relation $n_e \sim 1.2 n_{\rm H}$, we have $r = (L_{\rm ion}/n_{\rm H}\xi)^{1/2} \sim (2.2$–$5.2) \times 10^{17}$ cm, or ∼0.07–0.17 pc. For an $M_{\rm BH} \approx 10^9\ M_\odot$ appropriate for PDS 456 (R09, R14, Landt et al. 2013), this corresponds to a radius of ∼1500–3500 $r_{\rm g}$ from the black hole. This is comparable with inner regions of the BLR, at the order of ∼1000 $r_{\rm g}$ (O'Brien et al. 2005, R09) from the black hole. However, we note that this estimate is likely only the characteristic radius for the responding material. Should the outflow be stratified along the LOS (e.g., as in Tombesi et al. 2013) there could still be material over a large extended range of radii.

4.2. A Transiting Cloud

In the second scenario (our Model B), we showed that the absorption could also be modeled with a column density which increases from $\log(N_{\rm H}/{\rm cm^{-2}}) < 22.6$ to a maximum ∼23.8 over the course of the observation, with a constant $\log(\xi/{\rm erg\,cm\,s^{-1}}) \sim 3.45$. Detailed simulations of accretion disk winds have shown that their ejecta are often clumpy, with a complex density structure (e.g., Kurosawa & Proga 2009; Sim et al. 2010b; Takeuchi et al. 2013). If changes in column density are indeed responsible for the observed line variability in PDS 456, one possibility is that the changes could be associated with an inhomogeneous clump of material within a disk wind. Alternatively, the clump could originate in an outburst of material being blown from the disk surface during the flaring period.

Regardless of its origin, the linear extent (diameter) of a transiting clump can be estimated from $\Delta d_{\rm cloud} = v\Delta t$, where v_t is the cloud velocity tangential to the LOS and Δt is the total duration of the transit. Taking $\Delta t = 2 \times 400$ ks, corresponding

[8] Although noting the observations are not simultaneous.

to twice the time between the first definitive detection of the absorption in slice 5 and it reaching its maximum depth in slice 7, and making the reasonable assumption that $v_t \sim v_{out} \simeq 0.25$ c, we estimate $\Delta d_{cloud} \approx 6 \times 10^{15}$ cm (or ~40 r_g in PDS 456). Taking $\log(N_H/cm^{-2}) = 23.8$ (as measured in slice 7 when the absorption was deepest), and assuming that the absorbing cloud is spherically symmetric, we can then infer its density as $n_H = N_H/d_{cloud} \approx 1 \times 10^8$ cm^{-3}. This then leads to $r = (L_{ion}/n_H\xi)^{1/2} \sim (2.8\text{–}6.7) \times 10^{16}$ cm $\simeq$ 200–500 r_g, depending on whether the outflow is shielded or not.

Overall, the inferred wind properties are consistent with those posited by R14 after applying the Sim et al. (2008, 2010a) disk-wind model to the 2007–2011 *Suzaku* spectra. We also note the similarity between our estimated parameters for the wind and those recently predicted for a time-variable disk wind by Takeuchi et al. (2013). On the basis of R-MHD simulations, Takeuchi et al. show that a continuum-driven disk wind can become significantly clumpy or filamentary at $r \gtrsim 400\ r_g$ from the black hole, with the clumps having an optical depth τ of the order of unity, an ionization parameter $\xi \sim 10^3$ erg cm s^{-1} and an observational variability timescale of roughly one week. These values are similar to those found here for our Model B.

5. IMPLICATIONS FOR OUTFLOW ENERGETICS

Therefore the outflow in PDS 456 is constrained to lie between 200–3500 r_g from the black-hole, depending upon the model adopted and whether the gas is shielded. We now consider the energetics associated with such a wind. We first calculate the mass outflow rate using the expression $\dot{M}_{out} \equiv \Omega m_p N_H v_{out} r$, where Ω is a parameter which sets the overall wind geometry (in terms of the solid angle). This equation is the same as the one derived by Krongold et al. (2007), with $\Omega = (6/5)\pi$ being identical to their case of a vertically launched bi-conical wind with solar abundances that has an average angle of 30° with respect to the LOS (see Krongold et al. 2007 for details). Because $\dot{M}_{out} \propto r$ we consider here only the most conservative estimate of $r \gtrsim 200\ r_g$ as this will lead to a similarly conservative estimate on the wind energetics. As an aside, it is also important to note that the two limiting cases that we have considered in this work, i.e., that the wind is either shielded or unshielded from the full ionizing continuum by the partially covering gas, are likely to represent the absolute extreme scenarios. In the former case, should the shielding gas be ionized rather than neutral (as has been assumed here for simplicity), then the reduced gas opacity (and enhanced transmission) will allow a larger fraction of L_{ion} to be "seen" by the wind, thereby leading to a larger inferred distance r. The lower estimate of $r \simeq 200\ r_g$ considered here should therefore be regarded as extremely conservative; if a larger estimate on r was adopted instead, then the subsequent energetics will be correspondingly larger.

Thus, for a mean $\log(N_H/cm^{-2}) = 23.6$ (taken over slices 4–8) appropriate for our Model B, taking $r \gtrsim 200\, r_g \simeq 2.8 \times 10^{16}$ cm, and adopting $v_{out} = 0.25$ c, we conservatively estimate that $\dot{M}_{out} \gtrsim 5.3 \times 10^{26}$ g s^{-1} $\simeq 8\, M_\odot$ yr^{-1} in PDS 456. This can informatively be written in terms of the Eddington mass accretion rate, $\dot{M}_{edd} = L_{edd}/\eta c^2$, where $L_{edd} = 4\pi G m_p M_{BH} c \sigma_T^{-1} \simeq 1.26 \times 10^{38} (M_{BH}/M_\odot)$ erg s^{-1} is the Eddington luminosity and η is the accretion efficiency of the black hole. For our estimate on the mass outflow rate we find $\dot{M}_{out}/\dot{M}_{edd} \gtrsim 0.4(\eta/0.1)(M_{BH}/10^9 M_\odot)^{-1}$, which implies that the mass outflow rate is at least ~40% of the Eddington accretion rate for a reasonable $\eta = 0.1$. Similarly, we can estimate the wind kinetic luminosity in Eddington units as $L_{kin}/L_{edd} \gtrsim 1(v_{out}/c)^2(M_{BH}/10^9 M_\odot)^{-1}$, while the momentum rate of the flow is given by $\dot{p}_{out}/\dot{p}_{edd} \gtrsim 4(v_{out}/c)(M_{BH}/10^9 M_\odot)^{-1}$. For the values appropriate here, i.e., $M_{BH} \simeq 10^9 M_\odot$ and $v_{out} \simeq 0.25$ c, we hence estimate $L_{kin} \gtrsim 0.06 L_{edd}$. This corresponds to $\sim 8 \times 10^{45}$ erg s^{-1} which larger than the typical ~0.5%–5% of $L_{bol} (\equiv 10^{47}$ erg s^{-1} in PDS 456; Simpson et al. 1999; Reeves & Turner 2000) thought necessary for significant feedback (Di Matteo et al. 2005; Hopkins et al. 2010). Moreover, the momentum rate in the flow is comparable to that expected for the Eddington-limited photon field, i.e., $\dot{p}_{out} \gtrsim \dot{p}_{edd}$, which strongly suggests that the wind was radiatively accelerated by continuum-scattering processes and/or radiation pressure during an episode of near-Eddington-limited accretion, as has been argued by King & Pounds (2003) and King (2003, 2010).

Ultimately, while the overall wind energetics are likely sensitive to the overall flow geometry (e.g., Giustini & Proga 2012), these results imply a total integrated energy budget in the wind of $E_{out} \sim 10^{60}$ erg, for a representative quasar active phase of ~10^8 yr with a ~10% duty cycle. Thus, even in the *most conservative case*, the wind in PDS 456 could plausibly impart sufficient energy into the host galaxy to exceed the ~10^{59} erg binding energy of a mass 10^{11} $M_\odot$ galaxy bulge (with $\sigma = 300$ km s^{-1}). This supports the argument that the Fe K wind in PDS 456—and by extension those also observed in the wider AGN population (e.g., Tombesi et al. 2010, 2012; Gofford et al. 2013)—may play an important role in shaping the host galaxy through feedback.

6. ORIGIN OF THE ABSORBING GAS

Through this work, we have shown that despite the gradually increasing absorption at ~9 keV (rest-frame) being a defining characteristic of the last ~1 Ms of the 2013 *Suzaku* observation, the same absorption does not appear to be strongly present during the first ~400 ks. This raises an interesting question: where was the absorption at the start of the observation? We speculate briefly as to the reason for this on the basis of our two different absorption geometries. If the absorption is due to gas in photo-ionization equilibrium one possibility is that it is simply too highly ionized at the start of the observation to be observable in the spectrum. The light curve (Figure 4) shows that slice 1 traces a factor of ~2 decrease in source flux, perhaps following an even earlier flaring event. If this is the case, then the gas, having already been ionized by an earlier flare, may not have had time to sufficiently recombine into an observable feature before subsequently being re-ionized by the strong flare in slice 4. After slice 4, where there are no further strong flares, the gas may then have ample time to recombine, eventually giving rise to the the observed deep feature in slices 7–8.

Alternatively, should the absorption instead be due to a transiting inhomogeneous clump of gas, it is possible that the gas may not be present along the LOS at the start of observation. The onset of the absorption is first apparent in slice 4 which makes it tempting to speculate that the absorbing clump may be in some way related to the flare, perhaps, for example, being blown off of the disk by magnetic flaring in the Comptonizing corona and then further accelerated to high velocity by continuum scattering. Note that the observed outflow velocity of the gas corresponds to an escape radius of $r_{esc} = 2(c^2/v_{out}^2) \simeq 32\ r_g$ from the black hole. We could therefore be seeing the gas close to where it was launched from the disc, which lends weight to the idea that the absorption could be due to a clump of gas which occults the LOS.

7. CONCLUSIONS

This paper presents the first results from an extensive *Suzaku*, *XMM-Newton*, and *NuSTAR* observing campaign of powerful quasar PDS 456, occurring between 2013 February–September. We have reported on the remarkably variable high-velocity Fe K-shell wind which is evident in the new long (∼1 Ms duration) *Suzaku* observation. Consistent with earlier (2007, 2011) *Suzaku* observations, the wind is again detected through absorption at ∼9 keV in the source rest-frame ($v_{\rm out} \sim 0.25$ c). The absorption line depth increased by a factor of ∼5 during the new observation. This variability is equally well modeled by (1) an outflow in photo-ionization equilibrium which recombines in response to decreasing source flux, or (2) an inhomogeneous clump of gas which transits the LOS to the quasar. The variability allows us to directly determine the radius to the gas, e.g., as part of a clumpy outflow, which is constrained to lie between $r \sim 10^2 - 10^3\ r_{\rm g}$ of the black hole. Even in the most conservative case, the kinetic power of the flow is a significant fraction ($\gtrsim$6%) of the Eddington luminosity, and is comparable to the ∼0.5%–5% of $L_{\rm bol}$ thought necessary for significant feedback. The momentum rate of the flow is equivalent to the Eddington momentum rate which is consistent with the flow being radiatively accelerated by electron scattering during a near-Eddington-limited accretion episode.

We thank the anonymous referee for their comments and suggestions which helped improve the clarity of this manuscript. J. Gofford, J. N. Reeves, G. A. Matzeu, and M. T. Costa acknowledge financial support from the STFC. J.N. Reeves also acknowledges support from *Chandra* grant number GO1-12143X. This research has made use of data obtained from the *Suzaku* satellite, a collaborative mission between the space agencies of Japan (JAXA) and the USA (NASA).

REFERENCES

Bautista, M. A., & Kallman, T. R. 2001, ApJS, 134, 1
Bottorff, M. C., Korista, K. T., & Shlosman, I. 2000, ApJ, 537, 134
Chartas, G., Brandt, W. N., & Gallagher, S. C. 2003, ApJ, 595, 85
Di Matteo, T., Springel, V., & Hernquist, L. 2005, Natur, 433, 604
Dickey, J. M., & Lockman, F. J. 1990, ARA&A, 28, 215
Giustini, M., Cappi, M., Chartas, G., et al. 2011, A&A, 536, 49
Giustini, M., & Proga, D. 2012, ApJ, 758, 70
Gofford, J., Reeves, J. N., Tombesi, F., et al. 2013, MNRAS, 430, 60
Hopkins, P. F., & Elvis, M. 2010, MNRAS, 401, 7
Kaastra, J. S., Detmers, R. G., Mehdipour, M., et al. 2012, A&A, 539, 117
Kallman, T. R., Palmeri, P., Bautista, M. A., et al. 2004, ApJS, 155, 675
King, A. R. 2003, ApJL, 596, L27
King, A. R. 2010, MNRAS, 402, 1516
King, A. R., & Pounds, K. A. 2003, MNRAS, 345, 657
Koyama, K., Tsunemi, H., Dotani, T., et al. 2007, PASJ, 59, 23
Krongold, Y., Nicastro, F., Elvis, M., et al. 2007, ApJ, 659, 1022
Kurosawa, R., & Proga, D. 2009, ApJ, 693, 1929
Landt, H., Ward, M. J., Peterson, B. M., et al. 2013, MNRAS, 432, 113
McQuillin, R. C., & McLaughlin, D. E. 2013, MNRAS, 434, 1332
Middleton, M. J., Walton, D. J., Roberts, T. P., & Heil, L. 2014, MNRAS, 438, L51
Mitsuda, K., Bautz, M., Inoue, H., et al. 2007, PASJ, 59, 1
Nahar, S. N., Pradhan, A. K., & Zhang, H. L. 2001, ApJS, 133, 255
O'Brien, P. T., Reeves, J. N., Simpson, C., & Ward, M. J. 2005, MNRAS, 360, 25
Ohsuga, K., Mineshige, S., Mori, M., & Kato, Y. 2009, PASJ, 61, 7O
Pounds, K. A., Reeves, J. N., King, A. R., et al. 2003, MNRAS, 345, 705
Reeves, J. N., Braito, V., Gofford, J., & Sim, S. A. 2014, ApJ, 780, 45
Reeves, J. N., O'Brien, P. T., Braito, V., et al. 2009, ApJ, 701, 493
Reeves, J. N., O'Brien, P. T., & Ward, M. J. 2003, ApJ, 593, 65
Reeves, J. N., Porquet, D., Braito, V., et al. 2013, ApJ, 776, 99
Reeves, J. N., & Turner, M. J. L. 2000, MNRAS, 316, 234
Risaliti, G., Miniutti, G., Elvis, M., et al. 2009, ApJ, 696, 160
Risaliti, G., Nardini, E., Salvati, M., et al. 2011, MNRAS, 410, 1027
Sim, S. A., Long, K. S., Miller, L., & Turner, T. J. 2008, MNRAS, 388, 611
Sim, S. A., Miller, L., Long, K. S., Turner, T. J., & Reeves, J. N. 2010a, MNRAS, 404, 1369
Sim, S. A., Proga, D., Miller, L., Long, K. S., & Turner, T. J. 2010b, MNRAS, 408, 1396
Simpson, C., Ward, M., O'Brien, P., & Reeves, J. 1999, MNRAS, 303, 23
Takahashi, T., Abe, K., Endo, M., et al. 2007, PASJ, 59, 35
Takeuchi, S., Ohsuga, K., & Mineshige, S. 2013, PASJ, 65, 88
Tarter, C. B., Tucker, W. H., & Salpeter, E. E. 1969, ApJ, 156, 943
Tombesi, F., Cappi, M., Reeves, J. N., & Braito, V. 2012, MNRAS, 422, 1
Tombesi, F., Cappi, M., Reeves, J. N., et al. 2010, A&A, 521, 57
Tombesi, F., Cappi, M., Reeves, J. N., et al. 2013, MNRAS, 430, 1102
Wilms, J., Allen, A., & McCray, R. 2000, ApJ, 542, 914
Zubovas, K., & King, A. R. 2012, MNRAS, 426, 2751